Mass-gap control of Lorentzian graphene zero modes: Exact retuning, multiplet splitting, and local density of states resonances

Vahe Manukyan and Artur Ishkhanyan*
Institute for Physical Research, NAS of Armenia, Ashtarak 0204, Armenia

(Received 11 August 2026; revised 24 September 2026; accepted 28 October 2026; published 13 November 2026)

Smooth electrostatic wells in graphene can support normalizable states at the charge-neutrality (Dirac) point even though electrostatic confinement at nonzero energy is generally leaky. We examine how a spatially varying mass gap reorganizes this mechanism for a circular Lorentzian well under the explicit assumption that the localized mass and scalar potential are strictly coprofiled. A constant spinor-component rescaling gives an exact covariance of the radial equations at finite energy and background gap; the Lorentzian specialization then yields a closed critical-retuning law. The zero-mode manifold contains two regular angular families in each valley, and a weak uniform background gap produces opposite-sign slopes within a restricted localized-mass range, with asymmetric magnitudes when the localized mass is nonzero. Tail-corrected two-point shooting confirms the analytic slopes down to small background gaps and follows all six descendants of the $N = 4$ multiplet. The Lorentzian inverse-square tail additionally generates idealized geometric towers of near-edge states in supercritical low-angular-momentum channels. In a gapless exterior, the two angular sectors appear as paired local density of states resonances whose positions approach zero and whose widths collapse rapidly near criticality. These results connect exact coprofile covariance, zero-mode retuning, angular-pair splitting, threshold towers, and tunneling signatures within one two-dimensional Dirac model.

DOI: 10.1103/bbps-dcjq

I. INTRODUCTION

The low-energy carriers of monolayer graphene are governed by a two-dimensional Dirac equation, with sublattice pseudospin replacing the ordinary spin of relativistic quantum mechanics [1,2]. This structure is responsible for Klein tunneling and makes purely electrostatic confinement difficult at generic energies [3]. Circular gates nevertheless support quasibound states at finite energy, and at the Dirac point selected radial profiles can host square-integrable zero modes [4–6]. The latter are especially useful analytically because the threshold between a continuum resonance and a normalizable state can be followed without introducing a hard boundary.

The Lorentzian potential is a particularly transparent example. It is smooth at the origin, decays as the inverse square of radius, and approximates the broad potential created beneath a charged scanning probe or a smooth local gate [4,7]. For integer values of its dimensionless strength, the massless radial Dirac equation admits finite families of exact zero-energy states [5]. Their number and angular structure can be organized through shape invariance, while nearby finite-energy states appear as narrow local density of states (LDOS) resonances [4,5]. These results establish the zero-mode baseline used below.

Graphene mass gaps can arise from sublattice-asymmetric environments, including aligned hexagonal boron nitride (hBN), and may vary in space because of local stacking, strain, or patterned substrates [8–11]. A uniform gap changes the continuum threshold and permits true bound states inside the gap. A nonuniform gap is more than an additional scalar potential: it couples through the sublattice matrix and therefore probes the pseudospin polarization of each orbital. Spatially modulated gaps have previously been shown to confine Dirac carriers and to hybridize with electrostatically defined graphene dots [8,9]. The question addressed here is narrower and explicitly profile dependent: what becomes exact when the scalar potential and localized mass share the same radial envelope, and how does the resulting zero-mode structure appear in the discrete spectrum and the LDOS?

The central observation is an exact coprofile covariance. For a scalar term proportional to one radial envelope and a localized mass proportional to the same envelope, a constant rescaling of one radial spinor component removes the localized mass from the radial equations if the energy and uniform background mass are transformed linearly at the same time. This statement is not specific to a Lorentzian envelope. The Lorentzian becomes special because the transformed massless problem has known integer zero-mode thresholds and explicit wave functions. At zero energy and zero background gap, the covariance reduces to a closed critical-retuning law. The complete one-valley zero-mode manifold contains both $j > 0$ and $j < 0$ regular angular families. A weak uniform gap produces opposite-sign branches in the specified parameter range; outside it the slopes need not have opposite signs.

*Contact author: aishkhanyan@gmail.com

Published by the American Physical Society under the terms of the Creative Commons Attribution 4.0 International license. Further distribution of this work must maintain attribution to the author(s) and the published article's title, journal citation, and DOI.

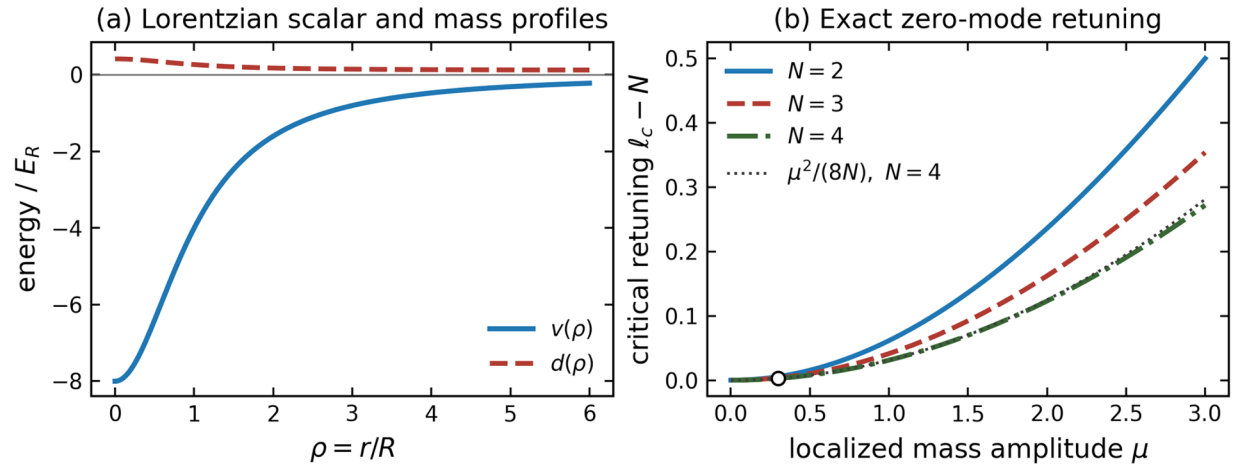


FIG. 1. (a) Dimensionless electrostatic potential $v(\rho)$ and mass profile $d(\rho)$ for $N = 4$, $\mu = 0.30$, $\ell = \ell_c$, and an illustrative $\delta = 0.12$. (b) Exact shift of the critical scalar strength over $0 \leqslant \mu \leqslant 3$ for three zero-mode families. Here N labels the massless integer family and ℓ_c denotes its retuned critical scalar strength, derived in Eq. (14). The open point marks $N = 4$, $\mu = 0.30$; the dotted curve is the quadratic small-μ approximation.

Correlated Lorentz-scalar and time-like-vector potentials are known to simplify Dirac equations, including spin/pseudospin-symmetry constructions and two-dimensional equal-potential models [12,13]. The covariance used here is related in spirit but is not an equal-potential symmetry limit. It is a component-rescaling identity for coprofiled scalar and mass terms. The Lorentzian retuning law, the paired angular splitting, and the threshold-tower structure derived below are consequences of applying that identity to the graphene radial problem.

Relative to the established massless Lorentzian solution [5] and general gap-defined confinement [8,9], the new content is therefore fourfold: an exact finite-energy coprofile covariance; the resulting Lorentzian critical-retuning law for the full two-sector zero-mode family; the analytic angular-pair splitting produced by a weak uniform gap; and the numerical connection of those states both to inverse-square near-edge towers in a gapped exterior and to LDOS resonances in a gapless exterior. The analysis is single particle, assumes smooth circular profiles and negligible intervalley scattering, and treats spin as passive. The second valley is restored by time reversal.

II. TWO-DIMENSIONAL DIRAC MODEL

For the K valley, the envelope Hamiltonian is

$$H_K = -i\hbar v_F(\sigma_x\partial_x + \sigma_y\partial_y) + V(r)I_2 + \Delta(r)\sigma_z. \tag{1}$$

Here $i^2 = -1$, $\hbar$ is the reduced Planck constant, v_F is the graphene Fermi velocity, $r = (x^2 + y^2)^{1/2}$, I_2 is the two-dimensional identity, and the Pauli matrices act on the A/B sublattice amplitudes. The signed Dirac mass energy is $\Delta(r)$, so the local band gap is $2|\Delta(r)|$. The K' Hamiltonian is obtained by time reversal. Because the profiles considered here do not break time-reversal symmetry, each state retains a degenerate valley partner.

Let R be the common radial range, define $\rho = r/R$, and introduce the Dirac energy scale $E_R = \hbar v_F/R$. The working profiles are

$$u(\rho) = \frac{1}{1+\rho^2}, \quad \frac{V}{E_R} = v(\rho) = -2\ell u(\rho),$$
$$\frac{\Delta}{E_R} = d(\rho) = \delta + \mu u(\rho). \tag{2}$$

Here $\ell > 0$ is the dimensionless scalar strength, $\mu = \Delta_L/E_R$ is the localized mass amplitude, and $\delta = \Delta_\infty/E_R$ is the asymptotic mass energy or background half-gap. Thus $\mu u(\rho)$ is the localized mass profile and δ is the uniform background contribution. The electrostatic depth at the origin is $V_0 = 2\ell E_R$, while the full band gap far from the dot is $2|\Delta_\infty|$. The numerical examples use $\mu > 0$ and, when present, $\delta > 0$. Figure 1(a) shows the profiles for the principal example.

Rotational invariance permits the spinor with integer m to be written as

$$\Psi_m(\rho,\varphi) = \frac{e^{im\varphi}}{\sqrt{2\pi}}\begin{pmatrix} f_m(\rho) \\ ie^{i\varphi}g_m(\rho)\end{pmatrix}, \quad j = m + \frac{1}{2}. \tag{3}$$

With $\epsilon = E/E_R$ and a prime denoting $d/d\rho$, the radial equations are

$$f_m' = \frac{m}{\rho}f_m - [\epsilon - v(\rho) + d(\rho)]g_m,$$
$$g_m' = -\frac{m+1}{\rho}g_m + [\epsilon - v(\rho) - d(\rho)]f_m. \tag{4}$$

The origin regularity has two sectors. For $m \geqslant 0$, the regular branch behaves as $f_m \sim \rho^m$ and $g_m \sim \rho^{m+1}$. For $m \leqslant -1$, the regular branch instead behaves as $f_m \sim \rho^{-m}$ and $g_m \sim \rho^{-m-1}$. Thus negative angular momentum is not an irregular branch; it supplies a second regular family. Time reversal exchanges $K \leftrightarrow K'$ and sends $j \mapsto -j$, or equivalently $m \mapsto -m-1$, but both signs of j already occur within a single valley. Smooth potentials suppress intervalley mixing, so each one-valley angular state has a degenerate partner in the other valley.

III. MASSLESS LORENTZIAN ZERO MODES

Set $\delta = \mu = \epsilon = 0$ and let $\ell = N \geqslant 2$ be an integer. For $p = 1, \ldots, N-1$, introduce $n = N-p-1$ and $z = \rho^2/(1+\rho^2)$. A convenient representative of the positive-j family is

$$f_{pN}^{(0)}(\rho) = \frac{\rho^p}{(1+\rho^2)^{p+1}}\, {}_2F_1(-n, p+1+N; p+1; z). \quad (5)$$

$$g_{pN}^{(0)}(\rho) = \frac{N\rho^{p+1}}{(p+1)(1+\rho^2)^{p+1}}\, {}_2F_1(-n, p+1+N; p+2; z). \quad (6)$$

The second regular family follows by component interchange,

$$\left(f_{-p-1,N}^{(0)}, g_{-p-1,N}^{(0)}\right) = \left(g_{pN}^{(0)}, -f_{pN}^{(0)}\right). \quad (7)$$

Because $-n$ is a nonpositive integer, both hypergeometric functions terminate. The two normalizable angular labels are therefore $m = p$ and $m = -p-1$, or equivalently $j = \pm(p+1/2)$. The channels $m = 0$ and $m = -1$ are marginal: their norms diverge logarithmically and they are not part of the normalizable zero-mode multiplet. Each valley consequently contains $2(N-1)$ normalizable zero modes, while the two valleys together give $4(N-1)$ orbital states before spin is included.

The two one-valley sectors also have a simple symmetry interpretation. For a vanishing Dirac mass, the effective single-valley antiunitary operator $\Theta = \sigma_2 \mathrm{K}$ commutes with the radial Hamiltonian, satisfies $\Theta^2 = -1$, and maps j to $-$j (m to $-m-1$), yielding the component interchange in Eq. (7). A Dirac mass is odd under this operation. Consequently, with nonzero mass the symmetry relates channel $-m-1$ at parameters (δ, μ) to channel m at $(-\delta, -\mu)$ at the same energy. At $\delta = \mu = 0$ the two angular sectors are therefore exactly degenerate at all energies; for finite mass the relation remains a useful analytical and numerical check. This symmetry is the origin of the two-sector degeneracy of the massless Lorentzian problem discussed in Ref. [5].

For the positive sector, $f_{pN}^{(0)} = O(\rho^{-p-2})$ and $g_{pN}^{(0)} = O(\rho^{-p-1})$ as $\rho \to \infty$; the negative sector has the same norm tail with the sublattice components interchanged. The radial norm density therefore behaves as $O(\rho^{-2p-1})$ in both sectors.

For compact notation, label the positive-j family as sector I and the negative-j family as sector II. With all states normalized, the sublattice norms satisfy

$$\frac{P_A^{\mathrm{I}}}{P_B^{\mathrm{I}}} = \frac{p}{p+1}, \quad \frac{P_A^{\mathrm{II}}}{P_B^{\mathrm{II}}} = \frac{p+1}{p}. \quad (8)$$

For both angular sectors, the Lorentzian-weighted sublattice imbalance vanishes,

$$I_{pN,s} \equiv \langle u(\rho)\sigma_z \rangle_{pN,s} = 0, \quad s = \mathrm{I}, \mathrm{II}. \quad (9)$$

Equation (8) follows directly from the terminated hypergeometric functions. Equation (9) can be verified by the same integrals; Appendix A gives the shorter Feynman-Hellmann argument from the exact critical curve.

IV. EXACT COPROFILE COVARIANCE AND LORENTZIAN ZERO-MODE RETUNING

The constant component rescaling is more general than the zero-energy limit. For any common radial envelope $u(\rho)$ in Eq. (2), define

$$g_m = c\tilde{g}_m, \quad c^2 = \frac{2\ell-\mu}{2\ell+\mu}, \quad \Lambda = \sqrt{\ell^2 - \frac{\mu^2}{4}}. \quad (10)$$

At the same time transform the energy and uniform background mass according to

$$\bar{\epsilon} + \bar{\delta} = c(\epsilon+\delta), \quad \bar{\epsilon} - \bar{\delta} = \frac{\epsilon-\delta}{c}. \quad (11)$$

For $|\mu| < 2\ell$, substitution into Eq. (4) gives

$$f_m{}' = \frac{m}{\rho} f_m - [\bar{\epsilon} + \bar{\delta} + 2\Lambda u(\rho)]\tilde{g}_m. \quad (12)$$

$$\tilde{g}_m{}' = -\frac{m+1}{\rho}\tilde{g}_m + [\bar{\epsilon} - \bar{\delta} + 2\Lambda u(\rho)] f_m. \quad (13)$$

Equations (12) and (13) are exactly the radial equations with no localized mass, scalar strength Λ, energy $\bar{\epsilon}$, and uniform mass $\bar{\delta}$. The identity is therefore an exact covariance for any coprofiled scalar and localized mass. It is not an isospectral map to one fixed transformed Hamiltonian when δ is fixed, because $\bar{\delta}$ depends on the physical eigenvalue through Eq. (11). The Lorentzian profile becomes special because its massless zero-energy thresholds are known exactly.

At $\epsilon = \delta = 0$, Eq. (11) gives $\bar{\epsilon} = \bar{\delta} = 0$. Normalizable Lorentzian zero modes therefore occur when $\Lambda = N$, which yields the exact critical retuning

$$\ell_c(N, \mu) = \sqrt{N^2 + \frac{\mu^2}{4}}, \quad N = 2, 3, \ldots. \quad (14)$$

At this retuned value, the transformed massless solutions (5)–(7) apply to both angular sectors. Before overall normalization, the positive sector has $(f, g) = (f_{pN}^{(0)}, c g_{pN}^{(0)})$, whereas the negative sector has $(f, g) = (g_{pN}^{(0)}, -c f_{pN}^{(0)})$. Thus the localized mass changes the relative sublattice weights but does not lift the zero-energy angular degeneracy.

For weak localized mass,

$$\ell_c = N + \frac{\mu^2}{8N} + O(\mu^4). \quad (15)$$

The retuning therefore begins at quadratic order. Consistent with Eq. (9), there is no first-order critical shift from the localized mass. At fixed ℓ, real c and Λ require $|\mu| < 2\ell$; along the retuned curve (14) this condition is automatically satisfied.

For the numerical calculations below we use $N = 4$ and $\mu = 0.30$. Equation (14) gives $\ell_c = 4.0028115$, while Eq. (10) gives $c^2 = 0.9277598$. Although the retuning of ℓ is small, the sublattice reweighting is linear in the localized mass and becomes visible once a uniform background gap is introduced.

V. ANGULAR-PAIR SPLITTING PRODUCED BY A BACKGROUND GAP

Switch on a weak positive background half-gap δ at the retuned critical point. The square-integrable zero modes make

the diagonal matrix element of $E_R\delta\sigma_z$ finite in every normalizable channel. Because the zero modes sit at the threshold of the gapless essential spectrum, we do not assume ordinary isolated-eigenvalue perturbation theory. Instead, the matrix element fixes the candidate right derivative at $\delta = 0$, and Sec. VI verifies that derivative by tail-corrected high-precision scaling.

Using Eq. (8) together with the B-sublattice rescaling in Eq. (10), the positive-angular sector has

$$\epsilon_{p,\mathrm{I}} = \delta\chi_{p,\mathrm{I}} + o(\delta), \quad \chi_{p,\mathrm{I}} = \frac{p-(p+1)c^2}{p+(p+1)c^2}. \tag{16}$$

The negative-angular sector has

$$\epsilon_{p,\mathrm{II}} = \delta\chi_{p,\mathrm{II}} + o(\delta), \quad \chi_{p,\mathrm{II}} = \frac{(p+1)-pc^2}{(p+1)+pc^2}. \tag{17}$$

Here $p = 1, \ldots, N-1$, with $m = p$ for the positive branch and $m = -p-1$ for the negative branch. In the absence of a localized mass,

$$\chi_{p,\mathrm{I}}(0) = -\frac{1}{2p+1}, \quad \chi_{p,\mathrm{II}}(0) = +\frac{1}{2p+1}. \tag{18}$$

Thus a uniform gap sends the two one-valley angular partners to opposite sides of zero energy only within the localized-mass range specified below. A nonzero localized mass preserves the common critical coupling but makes the magnitudes of the two slopes unequal. This $+j/-j$ asymmetry is a first-order spectral signature of the localized mass, whereas the critical retuning (15) begins only at second order.

For each $p = 1, \ldots, N-1$, Eqs. (16) and (17) have opposite signs precisely when $|\mu| < N/\sqrt{p(p+1)}$. At $|\mu| = N/\sqrt{p(p+1)}$ one slope vanishes; beyond that boundary both slopes have the sign of μ. Hence opposite signs for the complete multiplet require the sharper common condition $|\mu| < \sqrt{N/(N-1)}$. For example, at $N = 4$, $\mu = 2$, and $p = 3$, Eqs. (16) and (17) give $\chi_{3,I} = 0.1032561$ and $\chi_{3,II} = 0.3724869$, both positive. All six states in our $N = 4$, $\mu = 0.30$ example remain in the opposite-sign regime.

For $N = 4$ and $\mu = 0.30$, the coefficients are $\chi_{1,\mathrm{I}} = -0.2996021$, $\chi_{2,\mathrm{I}} = -0.1637536$, and $\chi_{3,\mathrm{I}} = -0.1059507$ for $m = 1, 2, 3$, together with $\chi_{1,\mathrm{II}} = +0.3662323$, $\chi_{2,\mathrm{II}} = +0.2357071$, and $\chi_{3,\mathrm{II}} = +0.1793706$ for $m = -2, -3, -4$. The corresponding states in the opposite valley have identical energies. Spin doubles every level again if Zeeman and spin-orbit terms are neglected.

The uniform and localized masses therefore play different spectral roles. The coprofiled localized mass enters the exact covariance and retunes the critical scalar strength. The uniform mass opens the exterior gap and probes the channel-dependent sublattice imbalance. In a real device these parameters need not be simultaneously tunable; Sec. VIII distinguishes the mathematical controls of the model from experimentally adjustable knobs.

VI. NUMERICAL IN-GAP SPECTRUM AND INVERSE-SQUARE THRESHOLD TOWERS

The full radial equations were integrated to test Eqs. (16) and (17) and to characterize the complete asymptotic structure. At the origin, the regular series was initialized according to the two Frobenius sectors described after Eq. (4). At large radius, retaining the Lorentzian $1/\rho^2$ tail is essential for shallow states. Eliminating g_m from Eq. (4) gives, to the first nonvanishing asymptotic orders,

$$f_m'' + \frac{1}{\rho}f_m' - \left[q^2 + \frac{\nu_m^2}{\rho^2} + O(\rho^{-3})\right]f_m = 0, \quad q = \sqrt{\delta^2 - \epsilon^2}. \tag{19}$$

The energy-dependent Bessel order is

$$\nu_m^2 = m^2 - 4\ell\epsilon + 2\mu\delta. \tag{20}$$

The decaying boundary condition is therefore $f_m \propto K_{\nu_m}(q\rho)$, with g_m/f_m obtained from the first Eq. (4). This reduces to the usual integer-order Bessel condition only when the inverse-square tail can be neglected. When $\nu_m^2 < 0$, the order is imaginary and the same K_{is} solution displays the logarithmic oscillation responsible for geometric threshold accumulation.

To count eigenvalues without losing very shallow levels, we also used a Prüfer phase. Writing $f_m = \mathcal{A}\cos\theta$ and $g_m = \mathcal{A}\sin\theta$ gives

$$\theta' = [\epsilon - v - d]\cos^2\theta + [\epsilon - v + d]\sin^2\theta - \frac{2m+1}{2\rho}\sin(2\theta). \tag{21}$$

The origin-regular phase and the phase propagated inward from the tail-corrected K_{ν_m} boundary were matched at $\rho_{\mathrm{match}} = 5$. Eigenvalues occur whenever their phase difference is an integer multiple of π, so the unwrapped phase provides an eigenvalue count in any chosen energy interval. Adaptive DOP853 integration used relative and absolute tolerances 2×10^{-11} and 2×10^{-13} respectively, for the broad parameter scans. The small-gap derivative test used substantially tighter tolerances, as summarized in Appendix B.

Figure 2 compares all six normalizable $N = 4$ descendants with the first-order slopes (16) and (17). The tail-corrected calculation resolves the $m = 1, 2, 3$ and $m = -2, -3, -4$ sectors at the displayed precision. The two sets move to opposite sides of zero energy, and their unequal magnitudes are the finite-μ angular-pair asymmetry predicted analytically. The corresponding numerical energies for all six descendants are listed in Table I.

The threshold nature of the $\delta = 0$ problem was tested directly by extending the calculation down to $\delta = 10^{-4}$. For each channel we monitored the scaled residual $R_m(\delta) = [\epsilon_m - \chi_m\delta]/\delta^2$. At $\delta = 10^{-4}$, R_m is finite and equals approximately 0.923, 0.326, 0.165, 0.852, 0.312, and 0.160 for $m = 1, 2, 3, -2, -3, -4$, respectively. Over the interval from 10^{-2} to 10^{-4} these quantities remain bounded. The slowest drift occurs in the $m = 1$ and $m = -2$ channels; no unbounded growth characteristic of a leading $\delta^2\log\delta$ term is resolved over this interval. The complete residual sequence is presented in Appendix B. These data provide high-precision numerical evidence for the right derivatives in Eqs. (16) and (17) and are consistent with a quadratic leading remainder over the resolved range, without excluding still higher-order nonanalytic terms. The algebraic zero-mode norm density also makes the far-tail contribution beyond the crossover scale higher order

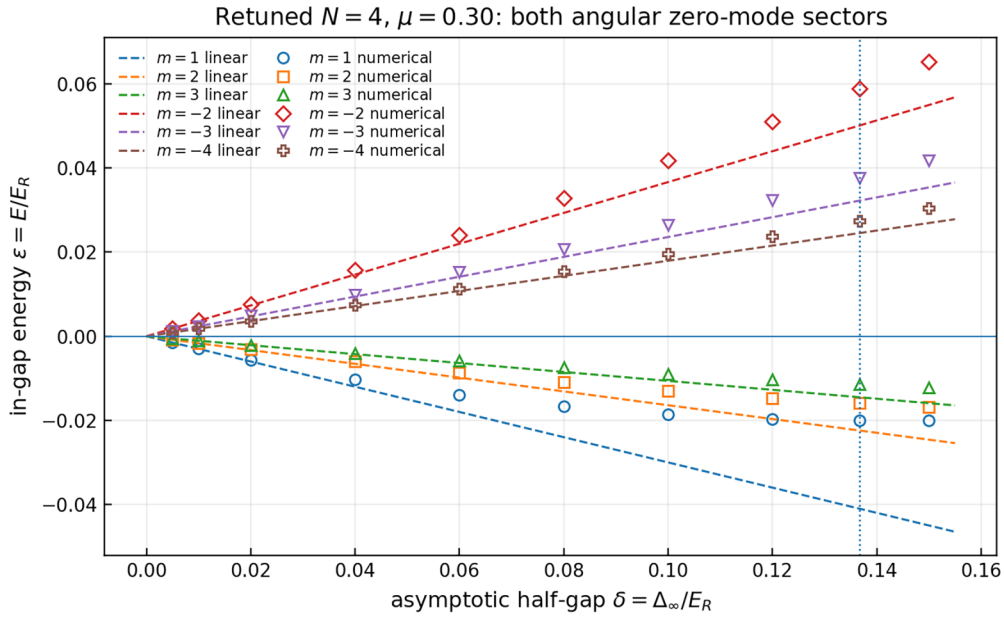


FIG. 2. In-gap energies of all six normalizable zero-mode descendants for the retuned $N = 4$, $\mu = 0.30$ dot. Open symbols are tail-corrected two-point-shooting results for $m = 1, 2, 3, -2, -3, -4$; dashed straight lines are the first-order slopes (16) and (17). The vertical dotted line corresponds to an asymptotic half-gap of 3 meV for $R = 30$ nm. The nonlinear bending at larger δ is a finite-gap correction, not a loss of the descendants.

than the linear term for every normalizable $p \geqslant 1$, supporting finite one-sided slopes.

For the physical example $R = 30$ nm, $v_F = 1.00\times10^6$ m/s, and $\Delta_\infty = 3$ meV, one has $E_R = 21.9404$ meV and $\delta = 0.136734$. The six descendants are $E_1 = -0.4403$ meV, $E_2 = -0.3491$ meV, $E_3 = -0.2489$ meV, $E_{-4} = +0.6024$ meV, $E_{-3} = +0.8235$ meV, and $E_{-2} = +1.2910$ meV. All lie well inside the 6 meV bulk gap. The smallest adjacent spacings within the descendant set remain 0.091 and 0.100 meV in the lower branch; the positive-energy branch is more widely separated.

The normalizable descendants are not the complete in-gap spectrum. The two marginal massless channels $m = 0$ and $m = -1$ require separate consideration for $\delta > 0$. At $\delta = 0.136734$, the $m = 0$ channel has a near-zero level at $\epsilon = 9.6506\times10^{-4}$. The $m = -1$ channel has no analogous near-zero level; its spectrum is discussed below together with the supercritical upper-edge sequence. These states are not

TABLE I. Weak-background-gap energies of all six normalizable zero-mode descendants at $N = 4$, $\mu = 0.30$, and $\ell = \ell_c$. Energies are in units of E_R. The signed relative deviation is computed from the absolute magnitudes; negative (positive) values mean that the numerical magnitude is smaller (larger) than the first-order value.

δ	m	Numerical ϵ_m	Linear value	Signed relative deviation (%)
0.005	1	−0.00147357	−0.00149801	−1.63
0.005	2	−0.00081058	−0.00081877	−1.00
0.005	3	−0.00052561	−0.00052975	−0.78
0.005	−2	0.00185120	0.00183116	1.09
0.005	−3	0.00118632	0.00117854	0.66
0.005	−4	0.00090086	0.00089685	0.45
0.010	1	−0.00289486	−0.00299602	−3.38
0.010	2	−0.00160467	−0.00163754	−2.01
0.010	3	−0.00104293	−0.00105951	−1.56
0.010	−2	0.00373903	0.00366232	2.09
0.010	−3	0.00238809	0.00235707	1.32
0.010	−4	0.00180971	0.00179371	0.89
0.020	1	−0.00556900	−0.00599204	−7.06
0.020	2	−0.00314283	−0.00327507	−4.04
0.020	3	−0.00205262	−0.00211901	−3.13
0.020	−2	0.00761080	0.00732465	3.91
0.020	−3	0.00483735	0.00471414	2.61
0.020	−4	0.00365134	0.00358741	1.78

members of the normalizable $N = 4$ multiplet; their placement reflects symmetry breaking caused already by the uniform mass, and is further modified by $\mu > 0$.

The uniform-mass contribution can be isolated by setting $\mu = 0$ while keeping $\delta = 0.136734$ and $\ell = 4$. Independent two-point integration then gives $\epsilon_{m=0} \simeq -0.00417960$ for the near-zero state and $\epsilon_{m=-1} \simeq 0.09428226$ for the deepest $m = -1$ state. Thus this angular-channel asymmetry does not originate exclusively from the localized mass: already $\delta \neq 0$ breaks the intravalley antiunitary relation at fixed parameters, while $\mu \neq 0$ introduces a further channel-dependent change. These marginal-channel levels remain distinct from the six normalizable $N = 4$ zero-mode descendants.

More importantly, Eq. (20) shows that the Lorentzian tail can become supercritical near the upper gap edge. As $\epsilon \to \delta^-$, the condition is $m^2 < 2\delta(2\ell - \mu)$. For the physical parameters, the right-hand side is 2.107, so $m = 0$ and $m = \pm 1$ are supercritical. Writing $\nu_m = is_m$, the small-q behavior of K_{is_m} produces an infinite geometric tower in the idealized unscreened model, with asymptotic ratio $q_{n+1}/q_n \to \exp(-\pi/s_m)$, or an energy-distance ratio $[\delta - \epsilon_{n+1}]/[\delta - \epsilon_n] \to \exp(-2\pi/s_m)$. The Prüfer count resolves this accumulating spectrum explicitly. In the window $q \geqslant 10^{-3}$ it finds two upper-edge levels in each supercritical channel: for $m = 0$, $\epsilon = 0.1301967$ and 0.1366385; for $m = 1$, 0.1334377 and 0.1367245; and for $m = -1$, 0.0969764 and 0.1365739. Further levels occur geometrically closer to $+\delta$. For example, in the $m = 0$ channel the ratio of the first two resolved energy distances from the upper edge is 0.0146, close to the asymptotic value 0.0132. At the lower gap edge the corresponding inverse-square order remains real, so no analogous geometric accumulation occurs. The $m = 0$ and $m = 1$ shallow roots are the deepest resolved members of their respective upper-edge towers. In the $m = -1$ channel, the deepest in-gap root is $\varepsilon = 0.0969764$; it is already the first resolved member of the same upper-edge tower.

The geometric accumulation assumes the inverse-square tail extends to arbitrarily large radii. The screened image-charge potential underlying Ref. [5] instead has a large-radius decay proportional to $2h_1h_2/r^3 + O(r^{-5})$, so screening or finite device size truncates the ideal accumulation. For the reported second $m = 1$ near-edge level, the decay length is $R/q \simeq 18.6\,\mu\text{m}$ at $R = 30\,\text{nm}$ (compared with $R/q \simeq 1.01\,\mu\text{m}$ for the first level). The very shallow tower levels are therefore model-dependent; the more localized zero-mode descendants are not generated by this asymptotic accumulation.

VII. GAPLESS EXTERIOR: PAIRED LDOS RESONANCES

When $\delta = 0$, nonzero-energy solutions are not truly bound because the exterior is gapless. The near-critical states can nevertheless be identified as resonances in the probability accumulated beneath a local probe. For positive energy, the far-field solution has the form

$$f_m \sim A_m J_m(\epsilon\rho) + B_m Y_m(\epsilon\rho),$$
$$g_m \sim A_m J_{m+1}(\epsilon\rho) + B_m Y_{m+1}(\epsilon\rho). \tag{22}$$

We normalize the scattering coefficients by $A_m^2 + B_m^2 = 1$. In the continuum convention of Ref. [4], the probe-integrated partial LDOS is

$$\mathcal{R}_m(\epsilon;\rho_p) = \frac{|\epsilon|}{2}\int_0^{\rho_p} \rho\left[f_m^2(\rho) + g_m^2(\rho)\right] d\rho. \tag{23}$$

We use $\rho_p = 5$. The coefficient normalization is a scattering convention, not delta-function energy normalization. An energy-independent probe factor changes only the peak height, whereas a slowly varying probe response leaves the peak position and probe-integrated LDOS full width at half maximum (FWHM) approximately unchanged in the narrow-resonance limit; this FWHM is not generally an intrinsic decay width.

The origin-regular solution was propagated to a far-field radius at least 30–35 oscillation lengths away and matched to both components in Eq. (22). The calculation includes both angular sectors. Equation (22) is retained as the free asymptotic normalization convention; Appendix B verifies the extracted peaks against a noninteger-order tail-corrected basis. Figure 3 shows the nearest pair, $m = 1$ and $m = -2$, at $\ell = 3.95$. Their peaks are close but not identical because the localized mass breaks the $+j/-j$ spectral symmetry away from zero energy.

At $\ell = 3.95$, the $m = 1$ resonance has $(\epsilon_r, \Gamma) = (0.0168763, 1.4154\times10^{-4})$, while its negative-angular partner $m = -2$ has $(0.0164544, 1.3801\times10^{-4})$. Figure 4 follows both branches as the scalar coupling approaches ℓ_c. The positions migrate nearly together, while the calculated LDOS FWHMs collapse by more than six orders of magnitude.

The LDOS FWHM should be distinguished from the intrinsic decay width $\Gamma_{\text{pole}} = -2\text{Im}\epsilon_{\text{pole}}$ of a pole continued to the outgoing-wave sheet. As a direct check, at $\ell = 3.70$, $\mu = 0.30$, $\delta = 0$, and $m = 1$, complex-scaled outgoing-wave matching yields $\epsilon_{\text{pole}} \simeq 0.07289109 - 0.01180928i$, or $\Gamma_{\text{pole}} \simeq 0.02361856$, whereas the probe-integrated LDOS FWHM is 0.0288521, about 22.2% larger. Their difference reflects the energy-dependent spectral background and the spatial probe integration for a broad, non-Lorentzian resonance. Figures 3 and 4 therefore report LDOS maxima and LDOS FWHMs; an identification with a pole width or a lifetime is justified only for isolated sufficiently narrow peaks.

For the $p = 1$ angular pair, the small-energy centrifugal behavior gives $\Gamma \propto \epsilon_r^3$ to leading order. A log-log fit to the four calculated points gives effective exponents 3.31 for both $m = 1$ and $m = -2$, consistent with the cubic threshold law rather than intended as a precision exponent measurement. The narrowest widths, near $\ell = 4.00$, are of order 1.4×10^{-8} and are LDOS width estimates; their identification with intrinsic pole widths requires sufficiently narrow, isolated resonances.

The higher angular pairs show the same hierarchy. At $\ell = 3.70$, the positive sector $(m = 1, 2, 3)$ has $(\epsilon_r, \Gamma) = (0.07623, 0.02885)$, $(0.15679, 0.004982)$, and $(0.24377, 0.0001648)$, while the negative sector $(m = -2, -3, -4)$ has $(0.07422, 0.02817)$, $(0.15427, 0.004902)$, and $(0.24096, 0.0001629)$. The paired channels are close in the gapless continuum, but the finite localized mass produces a small resolvable asymmetry in their resonance positions. The complete zero-mode family is therefore represented in the LDOS by three paired angular resonances rather than by only the positive-m sector.

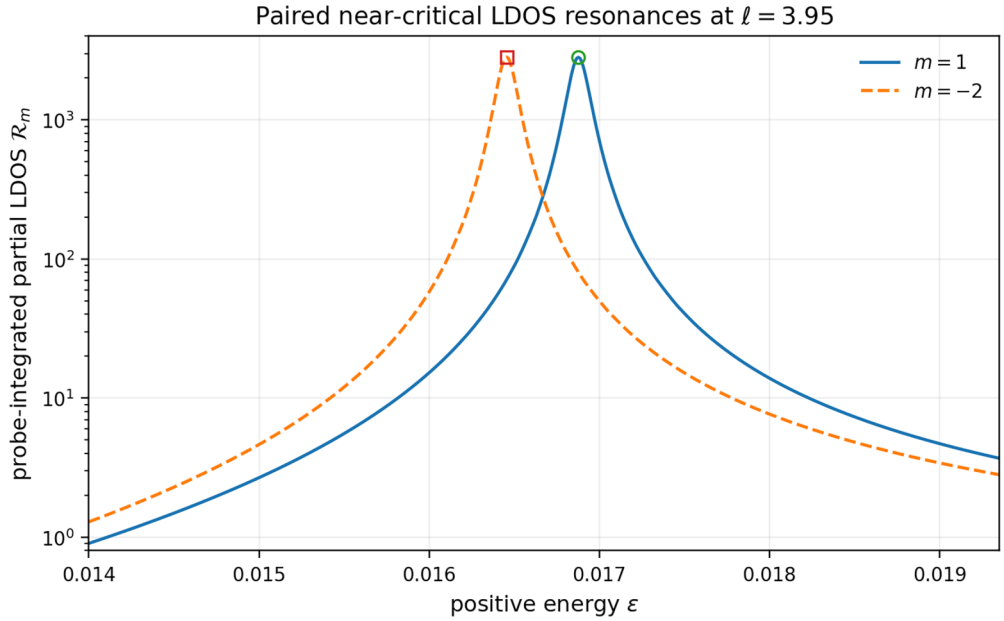


FIG. 3. Probe-integrated partial LDOS for the paired $m = 1$ and $m = -2$ channels at $N = 4$, $\mu = 0.30$, $\rho_p = 5$, and $\ell = 3.95$. Open symbols mark the numerical maxima. The resonance positions are 0.0168763 and 0.0164544, respectively; both converge to zero at $\ell = \ell_c$.

VIII. EXPERIMENTAL SCALES, TUNABILITY, AND INTERACTION EFFECTS

The conversion to physical units uses $\hbar v_F = 658.212$ meV nm for $v_F = 1.00\times10^6$ m/s. Table II lists three representative radii at $N = 4$ and $\mu = 0.30$. The localized mass amplitude is $\Delta_L = \mu E_R$, while the exact critical well depth is $V_{0c} = 2\ell_c E_R$. The resonance columns refer to the $m = 1$ channel at $\ell = 3.95$, for which $\epsilon_r = 0.0168763$ and $\Gamma = 1.4154\times10^{-4}$. The paired $m = -2$ values differ by only a few percent.

The required electrostatic depths of approximately 0.1–0.26 eV are within the scale created by charged tips and strong local gates in graphene spectroscopy, where circular quasibound-state patterns and discrete Dirac resonances have been imaged directly [7,14]. The localized quantities Δ_L in Table II are half-gap amplitudes and correspond to peak full gaps of approximately 7.9–19.7 meV, compatible with the millielectronvolt-to-tens-of-millielectronvolts gaps reported for graphene/hBN heterostructures [10,11]. The exact equality of the scalar and mass profiles is an idealization

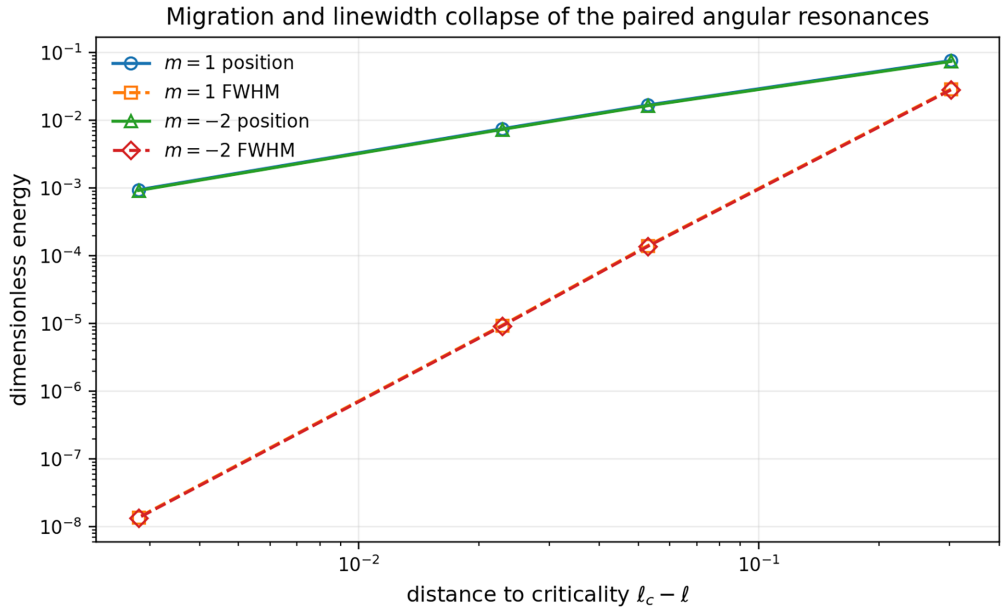


FIG. 4. Resonance position and probe-integrated LDOS FWHM versus distance from the retuned critical strength for the paired $m = 1$ and $m = -2$ channels. The four points correspond to $\ell = 3.70$, 3.95, 3.98, and 4.00. Both resonances become the corresponding square-integrable zero modes at $\ell = \ell_c$.

TABLE II. Physical scales for the $N = 4$, $\mu = 0.30$ family. The resonance quantities are evaluated for $m = 1$ at $\ell = 3.95$; V_{0c} denotes the retuned critical well depth.

R (nm)	E_R (meV)	V_{0c} (meV)	Δ_L (meV)	$E_{\rm res}$ (meV)	FWHM Γ_E (μeV)
20	32.91	263.5	9.87	0.555	4.66
30	21.94	175.6	6.58	0.370	3.11
50	13.16	105.4	3.95	0.222	1.86

defining the solvable benchmark. Unequal ranges do not obey the covariance (10)–(13) and require a separate numerical continuation.

The model parameters should not be read as a set of simultaneously tunable experimental knobs. The scalar strength ℓ is the natural *in situ* control because it follows a local gate or tip voltage, while R is set mainly by probe height and gate geometry. By contrast, the localized mass amplitude μ and its profile would usually be fixed during fabrication through local stacking registry, strain, or a patterned sublattice-asymmetric environment. The background mass δ could be supplied by global substrate alignment or another approximately uniform proximity mechanism, but in aligned monolayer graphene it is likewise generally fabrication defined. Their independence in the model means that they play distinct spectral roles and may be varied across device designs; it does not imply that every device provides independent continuous control of both mass scales.

For $R = 30$ nm, the $m = 1$ linewidth at $\ell = 3.95$ is 3.11 μeV, corresponding, in the isolated narrow-resonance (Breit-Wigner) approximation, to a lifetime of approximately 212 ps. The paired $m = -2$ resonance has $E_{\rm res} \simeq 0.361$ meV and a linewidth of approximately 3.03 μeV. These LDOS widths are narrower than the thermal and instrumental broadening of many tunneling measurements; disorder, phonons, and coupling to leads can broaden them further. The resonance position, gate-induced motion, and systematic angular linewidth hierarchy are therefore more robust observables than the inferred lifetime. In the gapped case, the smallest calculated descendant spacings are about 0.09–0.10 meV and call for sub-kelvin electron temperatures and low modulation voltages.

Electron-electron interactions modify the experimental interpretation but not the stated single-particle theorem for prescribed profiles. Long-range Coulomb interactions screen and self-consistently reshape the electrostatic potential, so the relation between an applied gate voltage and the parameters ℓ and R becomes device and filling dependent. They also add charging and exchange-correlation contributions to addition spectra. Short-range, including on-site-Hubbard, interactions can further lift spin or sublattice-related degeneracies in partially occupied shells and may generate filling-dependent mean-field shifts. A self-consistent Hartree or Hubbard mean-field treatment will generally generate scalar or staggered terms that are not exactly proportional to the prescribed Lorentzian envelope, so the coprofile covariance need not survive unchanged. These effects do not imply an interacting analog of Eqs. (10)–(14); rather, the present six-branch spectrum is the noninteracting orbital reference about which an interacting calculation must be built.

In transport, the charging scale $E_C = e^2/(4\pi\epsilon_0\epsilon_{\rm eff}R)$ is roughly 5–12 meV for a 30-nm dot with an effective dielectric constant between 4 and 10 before nearby-gate screening. This exceeds the smallest single-particle shell spacings calculated above. Coulomb-blockade addition spectra may therefore not reproduce the bare orbital separations directly; excited-state spectroscopy within a fixed charge state is the more appropriate transport comparison. Local tunneling spectroscopy provides a more direct probe of the calculated single-particle LDOS, although interaction-induced self-energy shifts and thermal broadening can still modify the observed peaks.

Atomic-scale disorder or sharp mass boundaries can mix valleys and remove the valley degeneracy assumed here. Nearest-neighbor trigonal warping breaks continuous rotational symmetry while preserving the particle-hole symmetry of pristine bipartite graphene. Next-nearest-neighbor hopping instead breaks that lattice particle-hole symmetry. The former affects angular-momentum-channel labeling; opposite-angular-channel degeneracy in a single valley relies on the massless intravalley antiunitary symmetry, while intervalley pairing follows from time reversal. None of these qualifications changes the exact coprofile covariance of the continuum one-body model, but all matter when fitting a specific device.

IX. CONCLUSIONS

A scalar potential and localized Dirac mass sharing one radial profile obey an exact covariance of the graphene radial equations: a constant rescaling of one spinor component removes the localized mass while linearly transforming the energy and uniform background mass. For the Lorentzian profile, the known massless zero-mode thresholds then give the exact retuning law $\ell_c = (N^2 + \mu^2/4)^{1/2}$. The Lorentzian is therefore the exactly solvable member of a broader coprofile covariance class.

The zero-mode manifold contains two regular angular families in each valley, $m = p$ and $m = -p-1$ with $p = 1, \ldots, N-1$. A weak uniform gap resolves them into opposite-sign branches only in the restricted localized-mass range specified after Eqs. (16) and (17). At zero localized mass the slopes are exactly antisymmetric; a finite localized mass preserves the common critical coupling while making the $+j$ and $-j$ slopes unequal in magnitude. Tail-corrected shooting confirms the six $N = 4$ descendants, and high-precision small-gap scaling provides numerical evidence for finite right derivatives at the threshold.

The Lorentzian $1/\rho^2$ tail adds a distinct spectral phenomenon. In sufficiently low angular channels the tail becomes supercritical near the upper band edge and produces infinite geometric towers in the idealized unscreened model

that are separate from the analytically controlled zero-mode descendants. A Prüfer-phase count resolves the near-edge levels and supplies a controlled way to enumerate states down to a chosen distance from threshold.

In a gapless exterior, the same two angular sectors appear as paired LDOS resonances. Their positions move toward zero and their probe-integrated LDOS widths collapse rapidly as the retuned critical coupling is approached. The solvable benchmark therefore links exact coprofile covariance, zero-mode retuning, angular-pair splitting, inverse-square threshold accumulation, and experimentally accessible resonance signatures. More realistic calculations with unequal scalar and mass ranges, screened electrostatics, disorder, or interactions can use this structure as a reference rather than as an assumption of independent *in situ* tunability.

ACKNOWLEDGMENTS

This work was supported by the Science Committee of the Republic of Armenia through Grant No. 25SC-CNR-1C003. During the preparation of this work, ChatGPT was used to assist with language, presentation, and algebraic and numerical cross checking. The authors reviewed and edited the resulting material and take full responsibility for the content of the publication.

V.M. and A.I. contributed to the conceptualization, methodology, analytical and numerical investigation, interpretation of the results, and preparation of the manuscript. Both authors reviewed and approved the final manuscript.

The authors declare no competing interests.

DATA AVAILABILITY

No external datasets were used. The numerical values reported in the figures and tables were generated directly from the equations stated in the manuscript. The numerical implementation is available from the corresponding author on reasonable request.

APPENDIX A: SUBLATTICE IDENTITIES AND THE SPLITTING COEFFICIENTS

Equation (8) follows from the terminated hypergeometric functions (5) and (6), and the negative-sector result follows from the component interchange (7). Along the exact critical curve $\ell = \ell_c(N, \mu)$, rotational symmetry keeps different m channels uncoupled. Applying the Feynman-Hellmann identity at $\mu = 0$ gives

$$0 = \left.\frac{d\epsilon}{d\mu}\right|_0 = \langle u\sigma_z\rangle - 2\left.\frac{d\ell_c}{d\mu}\right|_0 \langle uI_2\rangle = \langle u\sigma_z\rangle \qquad (24)$$

because Eq. (15) gives $(d\ell_c/d\mu)_{\mu=0} = 0$. At finite μ on the critical curve, Eq. (10) multiplies the transformed B-sublattice norm by c^2 in both angular sectors. Combining that rescaling with Eq. (8) gives the two coefficients in Eqs. (16) and (17).

TABLE III. Small-gap scaled residuals defined in Sec. VI for the six normalizable $N = 4$ descendants at $\mu = 0.30$ and $\ell = \ell_c$. The bounded sequences support finite right derivatives; their slow drift is not used to assign a unique second-order coefficient.

δ	R_1	R_2	R_3	R_{-2}	R_{-3}	R_{-4}
0.0100	1.0116	0.3286	0.1658	0.7671	0.3101	0.1601
0.0050	0.9774	0.3276	0.1657	0.8016	0.3112	0.1602
0.0020	0.9494	0.3270	0.1656	0.8284	0.3118	0.1603
0.0010	0.9375	0.3268	0.1656	0.8395	0.3120	0.1603
0.0005	0.9304	0.3267	0.1656	0.8461	0.3121	0.1603
0.0002	0.9254	0.3267	0.1656	0.8507	0.3122	0.1603
0.0001	0.9235	0.3266	0.1656	0.8524	0.3122	0.1603

APPENDIX B: NUMERICAL CHECKS

For the normalizable descendants, the origin-regular and exterior-decaying solutions were independently scaled and matched through the normalized determinant at $\rho_{\text{match}} = 5$. The outer condition used the energy-dependent order ν_m in Eq. (20), rather than the integer order m. Repeating the calculation with match points from 4 to 7, with 18–30 exterior decay lengths, and with tighter DOP853 tolerances changed the Table I levels by less than the last quoted digits. The tail-corrected condition leaves the well-separated $m = 1, 2, 3$ descendant energies unchanged at the displayed precision while remaining essential for a reliable count of the shallow near-edge states.

The threshold scaling was recomputed at $\delta = 10^{-2}$, 5×10^{-3}, 2×10^{-3}, 10^{-3}, 5×10^{-4}, 2×10^{-4}, and 10^{-4} using DOP853 relative and absolute tolerances of 10^{-12} and 2×10^{-14}, respectively, with the outer condition imposed at a radius of at least 30 decay lengths. The scaled residuals $R_m(\delta)$ are listed in Table III and remain bounded in all six channels. The slowest convergence occurs for $m = 1$, with additional slow drift in $m = -2$, but no unbounded growth characteristic of a leading $\delta^2 \log\delta$ remainder is resolved over the stated range. We therefore use these data as numerical evidence for the one-sided slopes, not as a proof of the complete higher-order expansion.

For the supercritical near-edge channels, the Prüfer phase (21) was unwrapped as a function of energy. Each crossing of an integer phase difference was counted once, avoiding the loss of roots as the levels accumulated geometrically. The quoted $m = 0$, $m = 1$, and $m = -1$ upper-edge levels are stable under changes of the matching radius and the outer phase. Extending the count to smaller q. produces further levels with ratios approaching the inverse-square asymptotic values stated in Sec. VI.

In the scattering calculation, the far-field coefficients were extracted from both spinor components. The resonance data were recomputed with outer phases corresponding to approximately 25–70 oscillation lengths and with successively tighter integration tolerances. As a tail check, the coefficient extraction was also repeated with the noninteger tail order from Eq. (20), specialized to $\delta = 0$ and with the lower component reconstructed from Eq. (4); at $\ell = 3.95$ the $m = 1$ and $m = -2$ peak positions shift by less than 2×10^{-9}. Reversing μ while interchanging $m = 1$ and $m = -2$ reproduces the paired resonance position to better than 10^{-9}, as required by

the antiunitary relation discussed in Sec. III. Peak positions and the quoted FWHM values are stable to at least four significant figures except for the ultranarrow $\ell = 4.00$ widths, which should be interpreted as LDOS width estimates; the intrinsic lifetime interpretation requires the narrow-resonance limit.

[1] A. H. Castro Neto, F. Guinea, N. M. R. Peres, K. S. Novoselov, and A. K. Geim, The electronic properties of graphene, Rev. Mod. Phys. **81**, 109 (2009).

[2] D. S. L. Abergel, V. Apalkov, J. Berashevich, K. Ziegler, and T. Chakraborty, Properties of graphene: A theoretical perspective, Adv. Phys. **59**, 261 (2010).

[3] M. I. Katsnelson, K. S. Novoselov, and A. K. Geim, Chiral tunnelling and the Klein paradox in graphene, Nat. Phys. **2**, 620 (2006).

[4] A. Matulis and F. M. Peeters, Quasibound states of quantum dots in single and bilayer graphene, Phys. Rev. B **77**, 115423 (2008).

[5] F. Correa, L. Inzunza, and V. Jakubský, Lorentzian quantum wells in graphene: The role of shape invariance in zero-energy-state trapping, Phys. Rev. B **110**, 075120 (2024).

[6] C. A. Downing, D. A. Stone, and M. E. Portnoi, Zero-energy states in graphene quantum dots and rings, Phys. Rev. B **84**, 155437 (2011).

[7] J. Lee, D. Wong, J. Velasco Jr, J. F. Rodriguez-Nieva, S. Kahn, H.-Z. Tsai, T. Taniguchi, K. Watanabe, A. Zettl, F. Wang, L. S. Levitov, and M. F. Crommie, Imaging electrostatically confined Dirac fermions in graphene quantum dots, Nat. Phys. **12**, 1032 (2016).

[8] G. Giavaras and F. Nori, Graphene quantum dots formed by a spatial modulation of the Dirac gap, Appl. Phys. Lett. **97**, 243106 (2010).

[9] G. Giavaras and F. Nori, Dirac gap-induced graphene quantum dot in an electrostatic potential, Phys. Rev. B **83**, 165427 (2011).

[10] J. Jung, A. M. DaSilva, A. H. MacDonald, and S. Adam, Origin of band gaps in graphene on hexagonal boron nitride, Nat. Commun. **6**, 6308 (2015).

[11] B. Hunt, J. D. Sanchez-Yamagishi, A. F. Young, M. Yankowitz, B. J. LeRoy, K. Watanabe, T. Taniguchi, P. Moon, M. Koshino, P. Jarillo-Herrero, and R. C. Ashoori, Massive Dirac fermions and Hofstadter butterfly in a van der Waals heterostructure, Science **340**, 1427 (2013).

[12] J. N. Ginocchio, Relativistic symmetries in nuclei and hadrons, Phys. Rep. **414**, 165 (2005).

[13] F.-L. Zhang, C. Song, and J.-L. Chen, Dynamical symmetries of two-dimensional systems in relativistic quantum mechanics, Ann. Phys. **324**, 173 (2009).

[14] C. Gutiérrez, L. Brown, C.-J. Kim, J. Park, and A. N. Pasupathy, Klein tunnelling and electron trapping in nanometre-scale graphene quantum dots, Nat. Phys. **12**, 1069 (2016).